Distribution and Evolution of CH$_4$, N$_2$, and CO Ices on Pluto's Surface: 1995 to 1998

W. M. Grundy and M. W. Buie

Lowell Observatory, 1400 W. Mars Hill Road, Flagstaff, Arizona 86001
E-mail: grundy@lowell.edu

We present new near-infrared spectra of the planet Pluto obtained at Lowell Observatory on 83 nights during 1995–1998. The dense temporal sampling of our observations enables us to measure with unprecedented detail cyclical changes in the depths of methane, carbon monoxide, and nitrogen ice absorption bands, modulated by Pluto's diurnal rotation. We show that CO, N$_2$, and weak CH$_4$ absorption band depths exhibit rotational patterns very different from those of Pluto's visible lightcurve, unlike the strong CH$_4$ absorption bands which are closely correlated with the visible lightcurve. Our observations are used to constrain the longitudinal distributions of the three ice species on Pluto's surface. The data also reveal a subtle, longer term strengthening of Pluto's strong near-infrared CH$_4$ bands, which is used to constrain the latitudinal distribution of CH$_4$ ice. We simulate the observed diurnal and seasonal spectral and photometric behavior of Pluto by means of model distributions of three terrain types. We see no evidence for changes in the distributions of Pluto's surface ices during the 1995–1998 interval. © 2001 Academic Press

Key Words: Pluto; ices; spectroscopy; surface evolution; volatile transport.

1. INTRODUCTION

The persistent visible lightcurve of Pluto (e.g., Marcialis 1997) implies a heterogeneous surface. Orbital and rotational circumstances ensure that different regions of Pluto's surface are oriented toward the Earth and Sun at different times. Over Pluto's day (6.4 Earth days), the sub-Earth and sub-Sun points on Pluto pass through all longitudes, enabling an observer on Earth to learn about the longitudinal distribution of Pluto's diverse terrains by studying how Pluto's spectral reflectance varies over that time period. Over longer, seasonal time scales, the sub-Earth and subsolar points on Pluto also move in latitude. In recent decades, these points have moved north from Pluto's southern hemisphere, crossing the equator during the mutual event season of the 1980s, and are now moving well into the northern hemisphere. If long-term variations can be disentangled from the shorter term longitudinal variations, pairs of observations taken at different epochs can be used to constrain the latitudinal distribution of terrains on Pluto.

Mapping Pluto's terrains in this fashion is considerably complicated by the fact that observable changes due to the changing illumination and viewing geometry can be difficult to distinguish from changes resulting from possible evolution of the surface of Pluto itself. Volatile ices on Pluto (thought to be primarily nitrogen, contaminated with CO, CH$_4$, and probably other minority constituents; see, e.g., Cruikshank *et al.* 1997) are in vapor pressure equilibrium with the atmosphere (see, e.g., Spencer *et al.* 1997). Energy is transported by sublimation and condensation with a bulk flow of gas from energy source to sink, leading to seasonal transport of volatile ices from regions receiving strong sunlight to areas receiving less, at rates possibly as high as several centimeters of ice removed or deposited per Earth year when Pluto is near perihelion, as it currently is (Spencer *et al.* 1997, Trafton *et al.* 1998, Grundy and Stansberry 2000).

During the past six years, we have pursued an intensive spectral and photometric monitoring campaign intended to search for changes due to both geometric and volatile transport effects. We have worked to obtain a densely sampled data set, hoping to distinguish between the different sorts of changes Pluto is expected to exhibit over time and to be able to use our observations to constrain models of the geographic distribution of Pluto's diverse terrains and of their evolution through time.

Our Pluto monitoring program makes use of all available telescope/instrument combinations. This paper reports results based on data obtained during the interval 1995–1998 with a single telescope and instrument. Restricting our analysis to this portion of the data set reduces the potential impact of systematic errors in our search for subtle secular trends.

2. DATA ACQUISITION AND REDUCTION

Data presented in this paper were all acquired at Lowell Observatory's 1.8-m Perkins telescope on Anderson Mesa. The instrument was OSIRIS, the Ohio State Infra-Red Imaging Spectrometer (described by DePoy *et al.* 1993). OSIRIS split the wavelength range from 1.2 to 2.4 μm into three orders by means of a grating and a cross-dispersing grism (grating–prism combination). These three orders, coinciding approximately with the J, H, and K atmospheric windows, were recorded simultaneously

on a 256×256 NICMOS3 HgCdTe array. We used a 3×54 arcsec slit, oriented North–South on the sky, resulting in spectral resolution of about 700. J band seeing at the Perkins telescope during 1995–1998 ranged from 1 to 3 arcsec, resulting in minor variations in slit losses during most nights.

Our observations yielded data of reducible quality on 83 nights, as tabulated in Table I, along with the mean sub-Earth latitude and longitude on Pluto and the total usable integration time on Pluto + Charon. The sub-Earth latitudes and longitudes are plotted in Fig. 1, showing the distribution of our spatial sampling of Pluto's surface. Each object observation consisted of one or more sets of at least five consecutive exposures, with individual exposure times ranging from 30 s for bright solar analog stars to 300 s for Pluto + Charon. For the brightest stars, shorter subexposures were used to avoid saturation. These were co-added to make synthetic 30-s exposures. Prior to each exposure, the object was moved to a new position in the spectrograph slit. This dithering compensated for the impact of individual bad pixels and permitted exposures to be subtracted pairwise to remove night sky lines. The optimal extraction procedures we used to extract spectra from OSIRIS spectral images have been described in detail by Grundy *et al.* (1999) and will not be further discussed here.

Stars were observed periodically, bracketing Pluto + Charon sequences in both time and airmass. Every third year, we selected a new 9th mag "Pluto star" near Pluto's position, with a B-V color matched to that of Pluto. Each night we observed the Pluto star, then Pluto + Charon, then the star again, and so on, alternating between the two. From the sequence of star observations, spectral extinction curves were derived for times appropriate to each Pluto + Charon observation. These were used to correct for telluric extinction effects. By dividing extinction-corrected Pluto + Charon spectra by extinction-corrected star
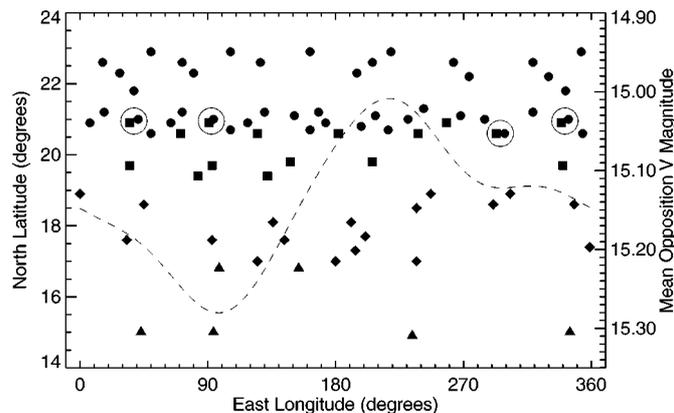

FIG. 1. Latitude and longitude of sub-Earth points on Pluto at times when our OSIRIS spectra were obtained, illustrating the density of our sampling of Pluto's surface. Observations during 1995, 1996, 1997, and 1998 are indicated by triangles, diamonds, squares, and circles, respectively. Pluto's visible lightcurve (dashed curve, right axis) gives an indication of the longitudes where visually brighter and darker materials occur on Pluto's surface. Circled pairs of observations are discussed in Section 4.2.

TABLE I
Summary of OSIRIS Pluto + Charon Observations

| UT date of observation | Phase angle (°) | Pluto's sub-Earth angle | | Total Pluto integration time (min) |
		Lon (°)	Lat (°)	
1995/03/13.5	1.78	154	16.8	115
1995/03/14.5	1.77	98	16.8	120
1995/06/18.4	1.01	94	15.0	45
1995/06/19.3	1.03	43	15.0	110
1995/06/20.3	1.06	345	15.0	100
1995/06/22.3	1.11	234	14.9	130
1996/03/01.5	1.88	0	18.9	45
1996/03/02.5	1.88	303	18.9	130
1996/03/03.5	1.87	247	18.9	85
1996/04/14.4	1.24	45	18.6	155
1996/04/15.4	1.21	348	18.6	180
1996/04/16.4	1.19	291	18.6	165
1996/04/17.4	1.16	237	18.5	160
1996/05/07.3	0.67	191	18.1	195
1996/05/08.3	0.64	136	18.1	75
1996/05/26.3	0.47	201	17.7	160
1996/05/27.3	0.48	144	17.6	135
1996/05/28.3	0.49	93	17.6	105
1996/05/29.3	0.50	33	17.6	185
1996/06/05.3	0.63	359	17.4	180
1996/06/08.2	0.70	194	17.3	45
1996/06/20.2	1.00	237	17.0	50
1996/06/21.3	1.03	180	17.0	55
1996/06/22.2	1.05	125	17.0	60
1997/03/21.5	1.73	258	20.9	135
1997/03/24.5	1.69	91	20.9	155
1997/03/25.4	1.68	35	20.9	170
1997/03/26.4	1.66	339	20.9	180
1997/04/15.4	1.27	293	20.6	195
1997/04/16.4	1.25	238	20.6	170
1997/04/17.4	1.23	182	20.6	130
1997/04/18.4	1.20	125	20.6	105
1997/04/19.4	1.18	71	20.6	215
1997/05/25.4	0.43	206	19.8	35
1997/05/26.3	0.43	148	19.8	265
1997/05/27.3	0.44	93	19.7	270
1997/05/28.3	0.44	35	19.7	270
1997/05/29.3	0.45	340	19.7	215
1997/06/08.4	0.62	132	19.4	45
1997/06/09.3	0.65	83	19.4	50
1998/03/08.4	1.87	219	22.9	130
1998/03/09.5	1.86	162	22.9	160
1998/03/10.5	1.86	106	22.9	160
1998/03/11.5	1.85	50	22.9	175
1998/03/12.5	1.85	353	22.9	185
1998/04/17.4	1.28	127	22.6	210
1998/04/18.4	1.26	72	22.6	215
1998/04/19.4	1.24	16	22.6	220
1998/04/20.4	1.21	319	22.6	215
1998/04/21.4	1.19	263	22.6	220
1998/04/22.4	1.17	206	22.6	205
1998/05/05.4	0.83	195	22.3	150
1998/05/07.4	0.78	80	22.3	120
1998/05/08.3	0.76	28	22.3	140
1998/05/09.4	0.73	330	22.2	220
1998/05/10.4	0.71	274	22.2	230
1998/05/27.3	0.42	38	21.8	255

Table I—*Continued*

UT date of observation	Phase angle (°)	Pluto's sub-Earth angle		Total Pluto integration time (min)
		Lon (°)	Lat (°)	
1998/05/28.3	0.42	342	21.8	240
1998/06/18.3	0.79	242	21.3	145
1998/06/19.2	0.81	168	21.2	150
1998/06/20.2	0.84	130	21.2	160
1998/06/21.3	0.87	72	21.2	100
1998/06/22.3	0.89	17	21.2	145
1998/06/23.3	0.92	319	21.2	95
1998/06/24.2	0.94	268	21.1	50
1998/06/25.2	0.97	208	21.1	140
1998/06/26.3	0.99	151	21.1	160
1998/06/27.3	1.02	94	21.0	195
1998/06/28.2	1.05	41	21.0	40
1998/06/29.2	1.07	344	21.0	145
1998/06/30.3	1.10	285	21.0	180
1998/07/01.2	1.12	231	21.0	165
1998/07/02.2	1.15	173	20.9	135
1998/07/03.2	1.17	118	20.9	150
1998/07/04.2	1.20	64	20.9	120
1998/07/05.2	1.22	7	20.9	125
1998/07/08.2	1.29	198	20.8	35
1998/07/14.2	1.42	217	20.7	40
1998/07/15.2	1.44	162	20.7	110
1998/07/16.2	1.47	106	20.7	120
1998/07/17.2	1.49	50	20.6	95
1998/07/18.2	1.51	354	20.6	120
1998/07/19.2	1.53	299	20.6	45

spectra, we removed instrumental effects as well. During 1995, we used SAO140910 for our Pluto star and we used SAO141142 during the three subsequent years.

Although located conveniently close to Pluto, our Pluto stars did not share the Sun's spectral energy distribution, so an additional correction was needed. The required information was obtained by observing well-known solar analogs such as BS 6060, 16 Cyg B, SA 102-1081, SA 105-56, SA 107-684, and SA 113-276. On most nights, we observed one or more of these stars, resulting in many independent determinations of the spectral differences between the Pluto stars and the solar analog stars. At the level of our ability to correct for telluric extinction and instrumental effects across our spectral range (several percent), all of these latter solar analog stars were seen to have identical spectral distributions. Pluto was nearest to BS 6060 in the sky, and so of the well-known solar analogs, this star was observed on the most nights. Our corrected Pluto + Charon spectra can thus be considered to be ratios to BS 6060, which is reported to be an excellent solar analog (see, e.g., Porto de Mello and da Silva 1997). To the extent that BS 6060 and the Sun have identical flux distributions, each corrected Pluto + Charon spectrum is proportional to the albedo spectrum of a body with the combined surfaces of Pluto and Charon. However, the constant of proportionality differs for each spectrum, due to variable spectrometer slit losses and changing phase angles.

After producing unscaled albedo spectra of Pluto + Charon, our next task was to remove Charon's spectral contribution so we could analyze spectra of Pluto alone. For the phase angle and longitude of each OSIRIS observation, we computed the combined Pluto + Charon fluxes at 1.57 and 2.125 μm (wavelengths were chosen as a compromise between the OSIRIS signal precision and the flatness of Pluto's lightcurve), using HST/NICMOS spectral observations of Pluto alone (Grundy and Buie, in preparation) and the separate phase coefficients of Pluto and Charon (Buie *et al.* 1997). Each OSIRIS Pluto + Charon spectrum was scaled to match these wavelengths. Then the Buie and Grundy (2000b) "standard model" Charon spectrum for the same geometry was subtracted, assuming radii of 1150 and 593 km for Pluto and Charon, respectively (Buie *et al.* 1997), to produce Pluto-only albedo spectra, for the geometry of each OSIRIS observation. Finally, we used Pluto's phase coefficient measured by HST/WFPC1 (Buie *et al.* 1997) to correct the Pluto-only spectra to A_1 albedos (defined the same way as the geometric albedo, except for phase angle $g = 1°$ instead of $g = 0°$, as described by Buie and Grundy (2000b)).

Note our dependence on ancillary data from HST/NICMOS and WFPC1. Without those data, we could have used the simpler Douté *et al.* (1999) procedure for removing Charon's spectral contribution. However, the significant difference between Pluto and Charon phase coefficients introduces phase-angle-dependent errors if they are not accounted for separately, as we have done. Though we attempt to overcome this source of error, our procedure still depends on many uncertain assumptions. For example, we do not know if the separate Pluto and Charon phase coefficients from Buie *et al.* (1997) are appropriate for all wavelengths. Our assumption that they are is buttressed by evidence that, for Charon, wavelengths between 1.4 and 2.5 μm exhibit very similar phase behavior, in spite of Charon's significant albedo contrasts over that wavelength range (Buie and Grundy 2000b). We also do not know if the assumed phase coefficients are appropriate for all regions of Pluto's heterogeneous surface. If either of these assumptions were problematic, we would be unable to proceed without considerably more dense temporal sampling and/or additional sources of data, such as densely sampled near-infrared filter photometry.

3. SPECTRAL FEATURES AND VARIABILITY

Example spectra are plotted in Fig. 2 to illustrate Pluto's spectral features in this wavelength range. Vibrational absorptions of methane ice dominate the spectral region, in spite of CH_4 perhaps being less abundant than nitrogen ice. N_2 ice is considerably less optically active than CH_4, and a correspondingly longer optical path length in N_2 ice is required to match the observed N_2 band at 2.15 μm (see, e.g., Grundy *et al.* 1993, Owen *et al.* 1993). The 0-3 overtone band of carbon monoxide ice is also seen in our spectra (Douté *et al.* 1999). Approximate absorption coefficients for the centers of selected absorption bands marked in Fig. 2 are
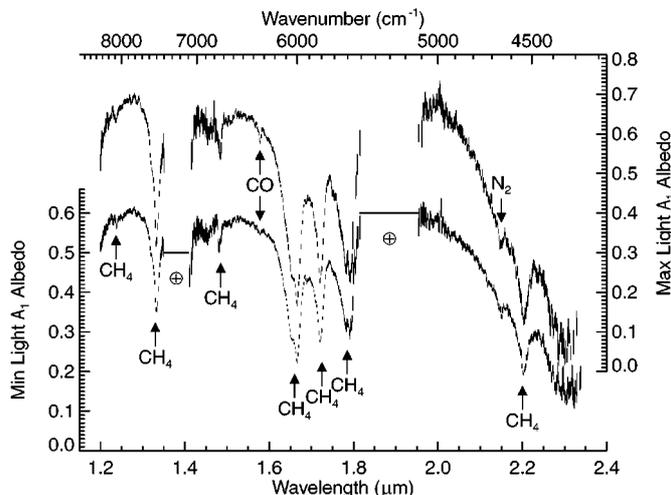
FIG. 2. Averages of OSIRIS Pluto spectra obtained near the minimum and maximum of Pluto's visible lightcurve. Ten spectra went into each average. The β nitrogen 0-2 band at 2.15 μm, the CO 0-3 band at 1.579 μm, and a number of CH$_4$ bands are marked with arrows. Areas blotted out by telluric water vapor absorptions are indicated by $\oplus$.

tabulated in Table II (the sources of these optical constants are described in the Appendix).

There are significant variations among our Pluto spectra, as is evident in Fig. 2, which shows deeper CO, N$_2$, and CH$_4$ bands and higher continuum albedos near the maximum of Pluto's visible lightcurve. In the remainder of Section 3 we will examine in greater detail the different types of variations exhibited by absorption bands of these three ice species.

3.1. CH$_4$ Absorption Bands

Quantitative analyses of Pluto's variable spectral features can be done by calculating ratios between strategically selected wavelengths for each night's data. This approach has the advantages of computational efficiency and minimizing sensitivity to scaling uncertainties. A ratio between the central wavelength of

TABLE II
Peak Absorption Coefficients of Selected Bands

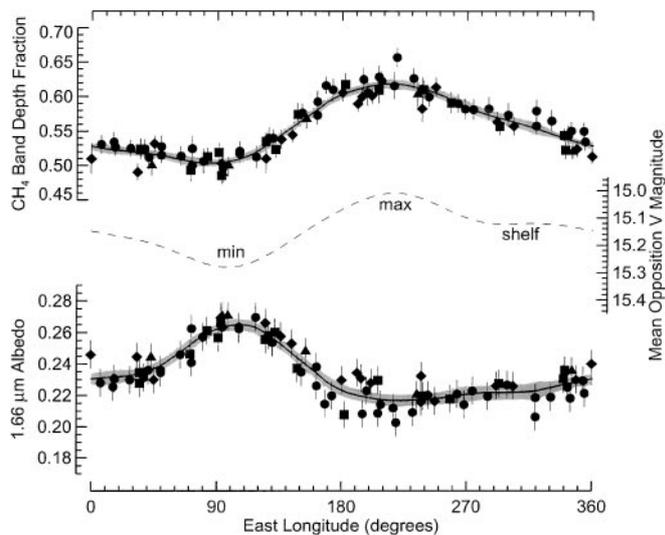| Ice species	Wavelength (μm)	Lambert absorption coefficient (cm^{-1})	Imaginary part of refractive index
CH$_4$	0.73	5.3×10^{-2}	3.1×10^{-7}
CH$_4$	1.24	4.9×10^{-2}	4.8×10^{-7}
CH$_4$	1.33	$5.2 \times 10^{+0}$	5.5×10^{-5}
CH$_4$	1.48	6.5×10^{-1}	7.7×10^{-6}
CH$_4$	1.66	$2.7 \times 10^{+1}$	3.6×10^{-4}
CH$_4$	1.72	$1.5 \times 10^{+1}$	2.1×10^{-4}
CH$_4$	1.79	$1.2 \times 10^{+1}$	1.7×10^{-4}
CH$_4$	2.20	$4.1 \times 10^{+1}$	7.2×10^{-4}
1% CO in β N$_2$	1.58	1.0×10^{-2}	1.3×10^{-7}
β N$_2$	2.15	1.5×10^{-2}	2.6×10^{-7}

FIG. 3. Band depth fraction of the 1.66 μm CH$_4$ band showing variation with sub-Earth longitude (top curve, upper left axis). The wavelengths used to compute this fraction were 1.655–1.665 μm (the CH$_4$ band) divided by the mean of 1.60–1.61 μm and 1.68–1.70 μm (the continuum). The solid curves with gray envelopes indicating uncertainty are LOWESS traces computed from the data (the procedure is described in the text). CH$_4$ absorption increases upward, with maximum CH$_4$ band depth corresponding to the visible lightcurve maximum. The 1996–2000 visible lightcurve (Buie and Grundy 2000a) is provided for reference, with longitudes associated with minimum and maximum light and "shelf" labeled (middle dashed curve, right axis). The bottom curve is the 1.66 μm band center A_1 albedo.

an absorption band and wavelengths adjacent to the band can be used to compute the fractional absorption depth of a specific band. Figure 3 shows the fractional band depth of the 1.66 μm CH$_4$ band, which can be seen to vary with Pluto's longitude. This particular band is deepest near Pluto's visible lightcurve maximum, shallowest near lightcurve minimum, and of intermediate depth in the intermediate "shelf" region of Pluto's lightcurve around 300° longitude.

The close correspondence between the visible lightcurve and the depth of the 1.66 μm CH$_4$ band implies that this absorption band is predominantly formed in the higher albedo material on Pluto's surface. It might be tempting to conclude from this curve that CH$_4$ ice *abundance* must also correlate with visible albedo, but such a deduction would be premature. The addition of minute amounts of an opaque continuum absorber can reduce both visible albedo and CH$_4$ band contrast with no appreciable change in the CH$_4$ abundance. If Pluto's lightcurve were caused by heterogeneous distribution of an opaque continuum absorber, almost all of the albedo variation would occur at continuum wavelengths. Association of CH$_4$ abundance with visual albedo also requires albedos at the center of CH$_4$ bands to be anticorrelated with visual albedo, which is approximately what is seen in our data, in the bottom panel of Fig. 3. The behavior of the band center albedo is as expected around minimum and maximum light, but subtle differences at shelf longitudes are intriguing, where the band center albedo is similar to the albedo

at maximum light. In contrast, the fractional band depth shows intermediate values at these longitudes, implying that CH_4 abundance could be just as high at shelf longitudes as it is at maximum light but that band depths and visible albedos at shelf are reduced by additional continuum absorption.

We examined comparable ratios and band center albedos for the CH_4 bands at 1.33, 1.72, 1.79, and 2.2 μm and all showed similar patterns with longitude, although with more scatter, due to poorer OSIRIS signal-to-noise performance at the absorption band and/or continuum wavelengths of these other methane features. The consistent longitudinal variation of band strengths for the strong CH_4 bands confirms and expands on earlier reports of correlation between Pluto's lightcurve and near-infrared CH_4 band depths (e.g., Marcialis and Lebofsky 1991).

However, an interesting contrast is provided by the weak CH_4 bands in high-albedo regions of Pluto's near-infrared spectrum. These weak absorption bands, having peak absorption coefficients some two orders of magnitude weaker than the stronger near-infrared bands (see Table II), are much more difficult to detect. However, two of them can be measured in the OSIRIS data, one at 1.24 μm and one at 1.48 μm. As shown by Fig. 4, there is considerable scatter in our measurements of their fractional band depths, but a distinctly different pattern can nevertheless be discerned in their longitudinal variation, with maximum absorption around longitude 0° and minimal absorption somewhere
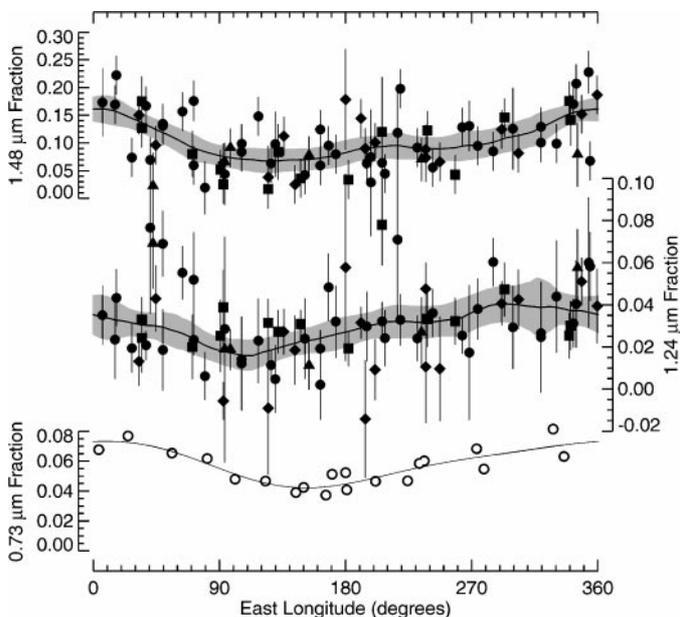
between minimum and maximum light. This pattern of band depth variation is similar to that reported from earlier observations of other weak CH_4 bands at wavelengths less than 1 μm (Buie and Fink 1987, Grundy and Fink 1996).

To extract curves representing longitudinal variations from the scatter of these data, we used the LOWESS (LOcally WEighted Scatterplot Smoothing, Cleveland 1979) algorithm. LOWESS is ideally suited for approximating the shape of an underlying curve from noisy, irregularly sampled data. Unlike polynomial or Fourier fits, LOWESS does not impose a functional form on the derived curve. The LOWESS trace is simply computed from the data, via low-order polynomial fits to the data within a moving window. For variations caused by different regions rotating in and out of view, the window must be relatively wide, because the underlying curves must vary gradually. For example, a point on Pluto's equator would be visible for exactly 180° of subviewer longitude, and the full width at half maximum of its longitudinal signature would be 120°. All LOWESS traces shown in this paper were computed with a 150°-wide triangular window, and a quadratic polynomial (windows ranging from 120° to 220° all gave similar results). Source code for our implimentation of the LOWESS algorithm is available from http://www.lowell.edu/users/buie/idl. We used a similar approach to estimate the uncertainty associated with each LOWESS trace, computing the standard error of the mean based on the formal errors of the data within a moving window.

The contrasting behaviors of weak versus strong CH_4 bands provides an essential clue toward understanding the distribution of CH_4 ice on Pluto. Methane is clearly not distributed as simply as one might conclude from only examining strong CH_4 absorption bands but must instead occur in at least two distinct reservoirs having different longitudinal distributions. It is the weak bands and not the strong bands which provide the better indication of CH_4 abundance, because the weak bands require significantly longer optical path lengths in CH_4 ice than are needed to form the strong CH_4 bands (approximate mean optical path lengths can be estimated by inverting the absorption coefficients in Table II). The weak bands can only form where methane is abundant, while the strong bands can form where methane is only a minority constituent. This point was initially explored by Grundy (1995) and by Grundy and Fink (1996) and will be examined in additional detail in Section 4.1 of this paper.

3.2. CH_4 Band Secular Evolution

A close examination of the upper curve in Fig. 3 reveals that the 1995 band depths (triangles) tend to plot slightly lower than the 1998 points (circles), suggesting that in addition to the longitudinal variations, the CH_4 absorption may have increased over that interval. We examined this possibility more quantitatively by comparing the entire set of band depths to a Fourier fit to the subset of the data obtained at sub-Earth latitudes between 20° and 22° (the most densely sampled latitude region). The band depths relative to the Fourier curve are shown for each of our 83 spectra in Fig. 5. When plotted against sub-Earth latitude
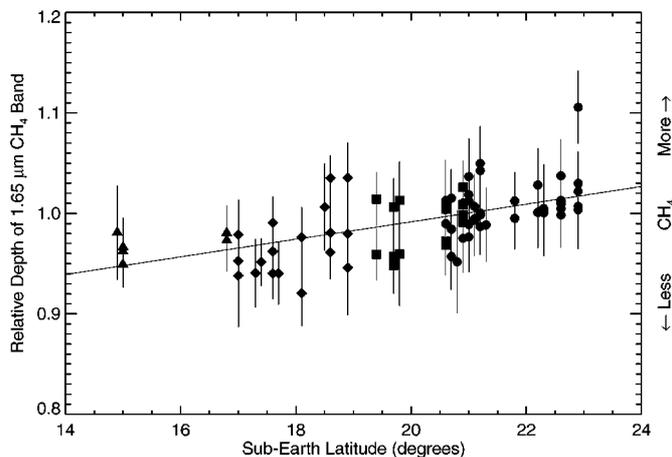

FIG. 4. Absorption fractions for weak CH_4 bands, with greater CH_4 absorption toward the top of the figure. From OSIRIS data we measured the $\nu_1 + 3\nu_4$ CH_4 band at 1.48 μm (top curve, upper left axis) and the unassigned CH_4 band at 1.24 μm (middle curve, right axis). Although the data are quite noisy, the LOWESS traces show significantly different longitudinal patterns from those of the strong CH_4 bands in Fig. 3 (see text). Also shown are Grundy and Fink (1996) data for the weak 0.73 μm band (open symbols, lower left axis, threaded by a Fourier fit to guide the eye), obtained during 1980–1994, at sub-Earth latitudes ranging from −9° to +14°.

FIG. 5. Increasing 1.66 μm methane band depth relative to a Fourier fit to all the data in the sub-Earth latitude interval 20–22° . Observation years are indicated with triangles, diamonds, squares, and circles, for 1995, 1996, 1997, and 1998, as in other figures. The straight line is a least-squares linear fit to the trend. The best fit slope is 0.88 ± 0.17 percent per degree of sub-Earth latitude.

(or against time) an increase in 1.66 μm CH$_4$ band depth with latitude (or time) appears to be confirmed.

If the apparent increase in 1.66 μm CH$_4$ band depth is real, other strong CH$_4$ bands should exhibit similar behavior. We did similar tests using the 1.33, 1.72, 1.79, and 2.2 μm bands. All five strong CH$_4$ bands showed increasing depth with latitude (and time), with best-fit slopes all larger than their 1σ formal errors. The measured slopes vary quite a bit from one band to the next, ranging from 0.30 to 0.88. The weighted average is 0.6 ± 0.1% per degree of sub-Earth latitude. These numbers depend on the spectral resolution and the wavelengths chosen for band and continuum windows and so presumably contain systematic errors. Future observations would be useful for refining these numbers, as they could benefit from the potential continuation of the trend over a longer time base.

Grundy and Fink (1996) searched for secular trends in CH$_4$ band depths, using CCD spectra obtained during 1980–1994 to measure CH$_4$ bands at 0.73 and 0.89 μm. Based on pairs of observations at three longitudes, separated by 7-year intervals, they reported that the 0.73 μm band became weaker (absolutely as well as relative to the stronger 0.89 μm band) with rates of decline ranging from 0.4 to 1.4 percent per degree of sub-Earth latitude.

That a weak CH$_4$ band shows the opposite secular trend from the stronger bands again implies that the weak and strong bands are formed in different provinces. It would be useful to test if weak CH$_4$ bands continue diminishing at present, simultaneously with the strengthening of the stronger CH$_4$ bands. Unfortunately, our OSIRIS signal precision is not sufficient to reveal band depth changes of only a few percent for such weak bands. Additional high signal-to-noise CCD and near-infrared spectral monitoring would be very useful for illuminating differences in secular evolution of weak and strong CH$_4$ bands, thus aiding differentiation

among the separate reservoirs of CH$_4$ ice responsible for producing the two classes of absorption bands.

3.3. CO Absorption Band

Carbon monoxide ice has been detected via absorption bands in Pluto's spectrum (Owen *et al.* 1993, Douté *et al.* 1999). From thermodynamic considerations and observations of the 0-2 overtone band at 2.35 μm, CO is thought to be dissolved as a minority constituent in Pluto's N$_2$ ice (e.g., Quirico and Schmitt 1997b, Douté *et al.* 1999). We were not able to observe the 0-2 CO band because OSIRIS provides insufficient signal precision at the wavelength of that band. However, the weaker 0-3 overtone at 1.579 μm is apparent in our spectra, revealing yet another pattern of longitudinal behavior, as shown by Fig. 6.

The 0-3 CO absorption reaches a relatively narrow maximum somewhere between minimum and maximum light, but it is nearly undetectable at shelf and 0° longitudes. This longitudinal pattern is reminiscent of the inverse of the pattern exhibited by the weak CH$_4$ bands, suggesting that CO is absent in terrains where CH$_4$ optical path lengths are longest. The relatively small longitudinal extent of the CO absorption peak and its much-reduced absorption strength away from its maximum are intriguing, suggesting that the terrain where this absorption band forms may be quite localized.

We only observed one CO band with OSIRIS, and so we could not use other absorption bands to confirm the observed behavior. Additional observations of the stronger 0-2 CO band would be useful for this purpose, although, being much stronger, that band will be more sensitive to highly diluted CO, and so its longitudinal distribution may be closely linked with that of N$_2$.

The OSIRIS data show no convincing evidence for secular evolution of the CO band, though the signal precision and brief
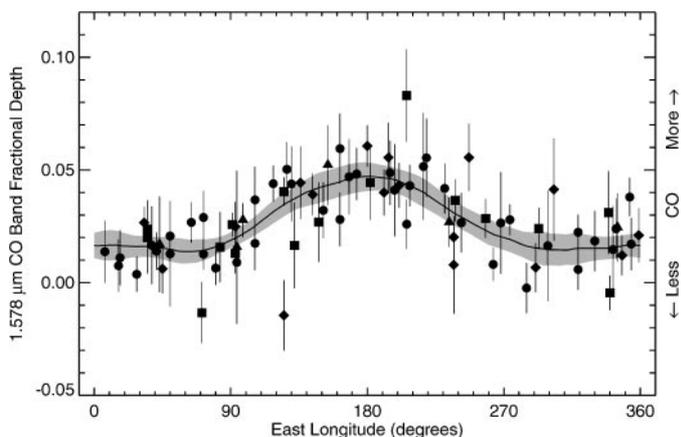

FIG. 6. Fractional band depth for the 0-3 CO band at 1.579 μm. The wavelengths used to compute these points were 1.577–1.581 μm (the CO band) divided by the mean of 1.561–1.576 μm and 1.582–1.597 μm (the continuum). Years are indicated with the plotting symbols used earlier and the solid curve enclosed in a gray envelope is the LOWESS trace.

time span do not permit particularly meaningful limits to be placed on the subtle changes which might be expected.

3.4. N₂ Absorption Band

We examined the weak nitrogen ice absorption band at 2.15 μm, which is produced by the 0-2 vibrational overtone transition in β N₂ ice (e.g., Grundy *et al.* 1993, Owen *et al.* 1993, Douté *et al.* 1999). Again, only a single N₂ band can be detected by OSIRIS, and so we cannot seek independent confirmation of our conclusions from other absorption bands. Measurement of this band is a difficult task for several reasons. OSIRIS signal precision declines at wavelengths beyond 2 μm, due to diminishing solar output, lower albedos on Pluto, and increasing sky background; as can be seen in Fig. 2, the 2.15 μm band is not a particularly striking feature in our data. Additionally, the N₂ band is located on the curved shoulder of the much stronger (and variable) CH₄ absorption band centered at 2.2 μm. Because these factors resulted in unacceptable levels of scatter when simple ratios were computed, we needed a more sophisticated approach.

We used a radiative transfer model based on Hapke theory (e.g., Hapke 1993) to fit the methane and nitrogen absorptions simultaneously, using as inputs 40 K infrared optical constants of β N₂ ice from Grundy *et al.* (1993) and of CH₄ ice from Schmitt *et al.* (1998). We chose a configuration consisting of a glaze of N₂ ice laying on top of granular CH₄ ice, consistent with recent volatile transport modeling by Grundy and Stansberry (2000). The best-fit N₂ glaze thickness results are shown in Fig. 7. As with the strong CH₄ ice bands, greater optical path lengths in N₂ ice are required near lightcurve maximum, but the longitudinal variation is seen to be somewhat different from the pattern shown by the strong CH₄ bands. Although N₂ absorption is somewhat reduced around minimum light, the minimum N₂ absorption seems to occur around 0° longitude, rather than near minimum light. This pattern is more like that exhibited by the CO ice band and is approximately the inverse of the weak CH₄ ice band pattern. Compared with the CO band, the N₂ absorp-
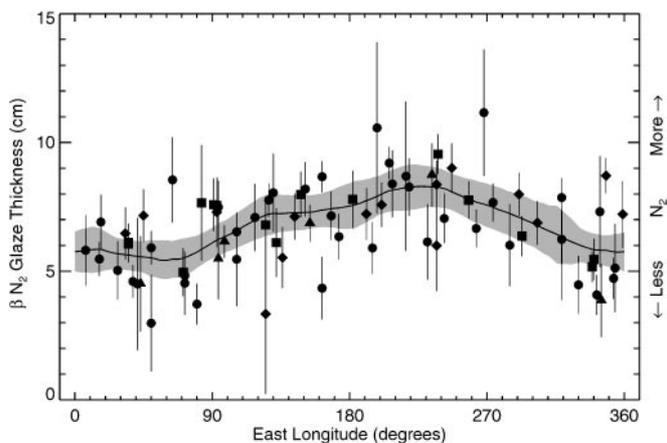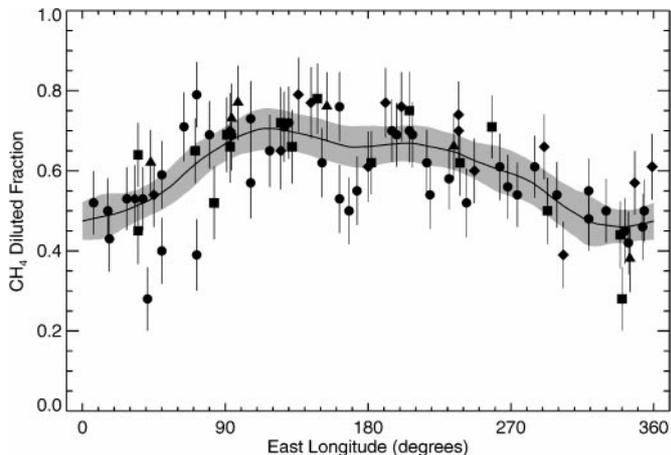
FIG. 8. Fraction of CH₄ diluted in N₂ ice computed from a Hapke model fit to the 1.66 μm CH₄ band. Observation years and the LOWESS trace are indicated as in previous figures.

tion diminishes by a smaller factor at longitudes away from its maximum, and the maximum appears to be more extended in longitude, implying that the regions producing the N₂ ice band on Pluto are more evenly distributed in longitude than the regions producing the CO band.

3.5. CH₄ Band Shifts

Methane absorption bands shift toward shorter wavelengths when the methane is highly diluted in nitrogen ice so that each CH₄ molecule is surrounded by N₂ molecules instead of other CH₄ molecules (Quirico 1995, Quirico and Schmitt 1997a, Schmitt *et al.* 1998). Douté *et al.* (1999) showed that, unlike on Triton, CH₄ on Pluto must be present in two phases, one diluted in N₂ ice and the other rich enough in CH₄ that the CH₄ crystal structure prevails. Thermodynamically, the coexistence of these two phases implies that methane is sufficiently abundant (greater than 3 to 5% relative N₂, depending on the temperature) to saturate the available N₂ ice, with excess methane forming CH₄-rich grains containing N₂ as the minority species (Trafton 1999). In this scenario, local ratios of the CH₄-rich and N₂-rich phases depend on the local relative abundances of CH₄ and N₂ ices.

More of the observed CH₄ might be expected to be diluted in N₂ at longitudes where N₂ is more abundant (where N₂ optical path lengths are greater). If so, the methane bands should be more shifted toward shorter wavelengths at those longitudes. We tested this hypothesis by fitting the CH₄ bands in our data with a Hapke model in which the fraction of CH₄ in CH₄-rich versus N₂-rich ice is a free parameter, using optical constants from Schmitt *et al.* (1998) for the CH₄-rich component and from Quirico and Schmitt (1997a) for the N₂-rich component. In spite of considerable scatter, the 1.66 μm band clearly shows a greater fraction of diluted CH₄ at longitudes similar to the longitudes where N₂ optical path lengths are greatest, as shown in Fig. 8. These fits also verify the conclusions of Douté *et al.* (1999), that a substantial fraction of Pluto's CH₄ exists in the CH₄-rich

FIG. 7. Nitrogen glaze thickness fitted to observed 2.15 μm band. Observation years and the LOWESS trace are indicated as in previous figures.

phase, unlike the situation on Triton's surface (e.g., Quirico *et al.* 1999).

To verify the pattern shown in Fig. 8, we applied the same technique to the other observed CH$_4$ bands. Similar patterns were clearly shown by fits to the 1.33 and 1.72 μm CH$_4$ bands, and by LOWESS analysis, we were marginally able to detect similar trends in fits to the 1.48 and 2.2 μm bands as well. For the 1.24 and 1.79 μm bands, the scatter was sufficient to obscure any pattern. These results indicate that more of the CH$_4$ responsible for forming Pluto's strong near-infrared absorption bands is diluted in N$_2$ ice at longitudes where N$_2$ ice is likely to be more abundant. Additionally, CH$_4$-rich ice appears to be more widespread at longitudes having less N$_2$ absorption.

3.6. Other Possible Variations

As can be seen in Table I, our data were obtained at phase angles $0.4° < g < 1.9°$. Some solar system objects exhibit opposition surges in this angular range while others do not. Based on the diverse behavior of solar system objects, one might expect to see variable photometric behavior for Pluto's surface, perhaps between different wavelengths or between different regions. If such an effect could be detected and quantified, it could provide valuable remote-sensing opportunities. Using Hubble Space Telescope near-infrared spectrophotometry of Charon, Buie and Grundy (2000b) were unable to detect any variation of Charon's phase function with wavelength. Nevertheless, we searched our data set for wavelength-dependent phase angle effects by taking groups of spectra obtained at similar longitudes and plotting various spectral ratios versus phase angle. We searched for geographically variable phase-angle effects by comparing the plots produced using groups of observations near minimum light, near maximum light, and near 0° longitude. Our data could have revealed these types of effects if they were as significant as ~10% per degree, but no evidence was found for such strong wavelength-dependent or regionally variable phase-angle effects.

Transient variations have been reported in Triton's spectrum (e.g., Buratti *et al.* 1999). Since Triton and Pluto share similar surface and atmospheric compositions, sizes, photometric properties, and heliocentric distances, whatever putative processes are responsible for short-term changes in Triton's spectrum could also be expected to operate on Pluto. Visible wavelength photometric monitoring of Pluto during 1995–1998 (Buie and Grundy 2000a) shows no transient variability in Pluto's B–V color of the sort reported for Triton. Nevertheless, we searched our OSIRIS data for evidence of any transient spectral variability on Pluto by directing our attention toward outlying points in all of the plots generated in doing the analyses presented in earlier sections of this paper. In all cases, we found that the outliers corresponded to nights in which factors such as equipment problems, poor weather, short integration times, nearby field stars, etc. reduced our confidence in the data. In fact, considering the richness of our sampling, the data provide rather strong evidence against any transient variability of Pluto's near-infrared spectrum dur-

ing 1995–1998 (excluding changes which arose and then reverted back to baseline behavior during September–February when Pluto was unobservable from Earth). It should be noted that OSIRIS spectra of Triton obtained over the same 1995–1998 time interval showed no evidence of variability in Triton's near-infrared spectrum (Hilbert *et al.* 1998, 1999), even while transient changes were reported in Triton's visible spectrum (Buratti *et al.* 1999). Perhaps the sorts of visible-wavelength changes reported for Triton are not accompanied by changes at near-infrared wavelengths.

4. SPATIAL AND TEMPORAL DISTRIBUTION OF ICES

The previous section demonstrated several distinct patterns of variable spectral behavior exhibited by Pluto. We now attempt to bring together these separate pieces of information to see what, taken together, they can tell us about the distribution of volatile species on Pluto's surface. Two classes of variation will be considered in turn: longitudinal/diurnal variations and latitudinal/seasonal variations. All of the diurnal variations can be assumed to be due to a fixed (at least on the 1995–1998 time scale) longitudinal distribution of ices on Pluto's surface. The more subtle seasonal variations must be due to the increasingly northerly viewing geometry, to the ongoing effects of volatile transport processes, or to some combination of the two.

4.1. Longitudinal Distribution

Several earlier investigations have considered the longitudinal distribution of Pluto's ice species (e.g., Buie and Fink 1987, Marcialis and Lebofsky 1991, Grundy 1995). Grundy and Fink (1996) showed that at least three distinct terrains were required by the combination of CCD spectra and mutual event photometry (a conclusion also reached by Douté *et al.* (1999) from modeling Pluto's near-infrared spectrum). Slicing the Buie *et al.* (1992) maximum entropy albedo map into three levels, Grundy and Fink (1996) produced a hypothetical map for the geographic distribution of these three terrains. They used arguments about the effects of physical processes thought to be acting on Pluto's surface ices to characterize the terrains as follows. The darkest regions, mostly concentrated from 80° to 160° longitude, were postulated to consist of a dark, reddish lag deposit of water ice and organic *tholin* residues, with a spectrum reminiscent of 5145 Pholus. The brightest regions, concentrated at high latitudes and limited equatorial outcrops between 170° and 220° longitude, were composed of volatile nitrogen ice, with minor CH$_4$ and CO contamination, perhaps similar to the surface of Triton. The intermediate albedo slice was assumed to be dominated by CH$_4$-rich ice, with minor tholin contamination. This CH$_4$-rich unit was generally confined to lower latitudes and longitudes from 220° to 80°, and its existence was justified by volatile transport models (e.g., Benchkoura 1996, Stansberry *et al.* 1996, Trafton *et al.* 1998). The Grundy and Fink (1996) map was not proposed as a unique solution required by the available data. Rather, it was intended to demonstrate that such a

distribution could indeed reconcile the spectral and photometric data and to motivate folding together additional data sets capable of constraining more aspects of the problem.

Lellouch *et al.* (2000) advanced the effort to constrain the longitudinal distribution of Pluto's terrains significantly by obtaining lightcurves at several thermal infrared wavelengths from ISO. Using thermal models, Lellouch *et al.* (2000) showed that Grundy and Fink (1996) style 3-terrain maps are consistent with the thermal emission lightcurves, if in the darker two terrains thermal inertias are low enough that diurnal temperature variations are significant.

The OSIRIS data presented in this paper provide additional information about the distribution of Pluto's terrains. These data are particularly valuable for demonstrating the different behavior of weak and strong CH_4 bands and for directly measuring CO and N_2 ice absorptions (rather than inferring their distribution from marginally detected CH_4 band wavelength shifts, as done by Grundy and Fink (1996)). Figure 9 shows schematically how the longitudinal trends in our new data compare with each other and with the visible lightcurve.

As Fig. 9 shows, absorption in the strong CH_4 bands is distributed similarly to Pluto's visible lightcurve, implying that

these stronger bands are produced in the highest albedo terrain. The pattern shown by weak CH_4 bands could be described as similar, except for significantly reduced absorption around lightcurve maximum. The longitudes where weak CH_4 bands show diminished absorption relative to the stronger bands are about the same longitudes which show maximum N_2 and CO ice absorption and maximum CH_4 dilution in N_2 ice. Taken together, these trends suggest the following distribution of ices: least volatile ices near minimum light, most N_2 (with CH_4 and CO diluted in it) near maximum light, and most CH_4 near $0°$ longitude. This distribution of ices matches that proposed by Grundy and Fink (1996), based on a completely independent data set.

The dashed curves in Fig. 9 show the trends predicted by the Grundy and Fink (1996) map and the dotted curves show the same for the variant of that map proposed by Lellouch *et al.* (2000). The specific terrain models used to compute these model curves are described in the Appendix. Considering the limited spectral data used to constrain these maps, they do a surprisingly good job of predicting the longitudinal spectral variations seen in our OSIRIS data. However, significant deviations are evident. The discrepancies are particularly notable at longitudes near $90°$ and $270°$, where the models do not have enough N_2 absorption and have too much weak CH_4 absorption.

The Buie *et al.* (1992) albedo map which was used to produce the Grundy and Fink (1996) and Lellouch *et al.* (2000) maps was based partially on photometric observations of superior mutual events during the 1980s. These events offered a unique opportunity to map Pluto's sub-Charon hemisphere (centered at $0°$ longitude), but the tightly constrained orientation of Pluto during superior events made it difficult to distinguish between center-to-limb photometric effects and intrinsic albedo variations. Uncertainties in Pluto and Charon radii and radiative transfer in Pluto's atmosphere compounded the problem. These factors increase uncertainty about albedo features in the Buie *et al.* (1992) map at $90°$ and $270°$ longitudes, which were always positioned near the limb of Pluto during the mutual events.

To test if discrepancies between the Grundy and Fink (1996) map and the OSIRIS data could be traced to limb artifacts in the Buie *et al.* (1992) albedo map, we needed a Pluto map obtained independently of the mutual events. Fortunately, it has recently become possible to map Pluto's surface features by means of direct imaging, using observations at different longitudes to resolve ambiguities between albedo and limb effects. A series of Hubble Space Telescope WFPC2 observations of Pluto + Charon was obtained in 1994, leading to new visible and ultraviolet albedo maps (a preliminary analysis of the HST images was presented by Stern *et al.* (1997), but we make use of a newer version currently being prepared for publication). In a procedure analogous to that of Grundy and Fink (1996), we sliced this new HST map into three visual albedo levels and assigned them to similar compositional units. The HST map is shown in Fig. 10, along with other maps discussed in this paper. The longitudinal behavior of the HST map is very similar to
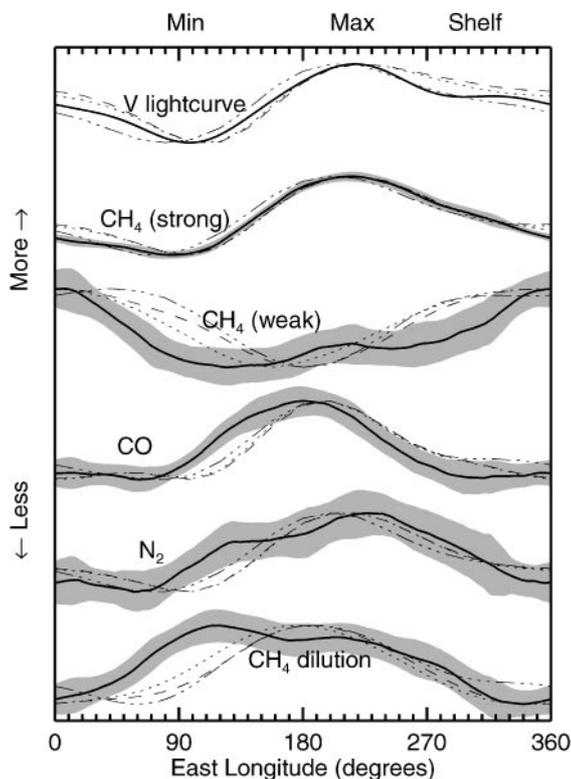

FIG. 9. The Buie and Grundy (2000a) 1996–2000 V lightcurve and longitudinal trends seen in OSIRIS data (solid curves with error envelopes). Longitudes "Min," "Max," and "Shelf" are indicated on the top axis. All curves are normalized to a common scale and oriented such that up is more (i.e., more light, more absorption, more dilution, etc.). The dotted, dashed, and dashed-dotted curves represent the behavior of Grundy and Fink (1996), Lellouch *et al.* (2000), and sliced HST maps, respectively, for sub-Earth latitude $22°$. These maps are shown in panels 1, 2, and 4 of Fig. 10.

that of the maps based on Grundy and Fink (1996), as indicated by the dashed-dotted curve in Fig. 9, bolstering the case that the features in the earlier maps near 90° and 270° are mostly real and that the failure of all three maps to replicate Pluto's longitudinal behavior should be blamed on something else.

We experimented with modifying the three-terrain maps, using information from OSIRIS data to guide where the extent of one terrain ought to be expanded at the expense of another. Because the OSIRIS data only provide approximate longitudinal information and extremely limited latitudinal information, any map created in this fashion depends heavily on human judgment and is necessarily somewhat arbitrary. Nevertheless, this exercise is useful for exploring the general implications of the trends exhibited by the OSIRIS data. We began with the Lellouch *et al.* (2000) version of the Grundy and Fink (1996) map and replaced some of the H$_2$O/tholin- and N$_2$-rich terrains around 0° longitude with CH$_4$-rich material. We also replaced some of the CH$_4$-rich terrain near 90° and 270° with H$_2$O/tholin and N$_2$. The modified map is shown in the fifth panel of Fig. 10, and the longitudinal trends predicted by it are plotted as dashed curves in Fig. 11. This map provides somewhat better matches to the behaviors of both weak and strong CH$_4$ bands, as well as to the N$_2$ band and the visible lightcurve.

We also created a map based on the HST data described earlier. For this map we permitted regions to be composed of "checkerboard" mixtures of different units, rather than forcing them to be homogeneously composed of a single unit, enabling us to achieve a closer match to the original HST albedo map. Our modified HST map is shown in the bottom panel of Fig. 10, and its longitudinal trends are indicated by dotted curves in Fig. 11. Examples of model spectra computed for this map are shown in Fig. 12, along with averaged OSIRIS spectra for similar viewing geometry. The longitudinal spectral behavior of this map is quite similar to that of the modified Grundy and Fink map. It is useful to consider the differences between these maps. Differences of this magnitude are unconstrained by the OSIRIS data. The mutual event maps should be more reliable near 0° longitude, while the HST map is preferred at longitudes away from 0°. Features shared by both maps are probably real; other features should be treated with skepticism.

A notable discrepancy which we were unable to overcome is seen between the CO absorption curve and both modified map models. Our model curves invariably show too much CO absorption at longitudes around 270°. This problem arises because CO and N$_2$ only occur together in our three-terrain models, and we need N$_2$ to be abundant at that longitude. It does not seem to be possible to reconcile the CO band depth curve with the other observed band depth curves, using a 3-terrain model with terrains like those described by Grundy and Fink (1996), where N$_2$ and CO always ocurr together. The N$_2$ and CO longitudinal curves differ in three important ways. They peak at different longitudes, their peaks have different widths, and their ratios between maxima and minima differ significantly (see Figs. 6 and 7). The OSIRIS data thus provide the first tentative evidence for either the existence of a fourth terrain type on Pluto or of longitudinal
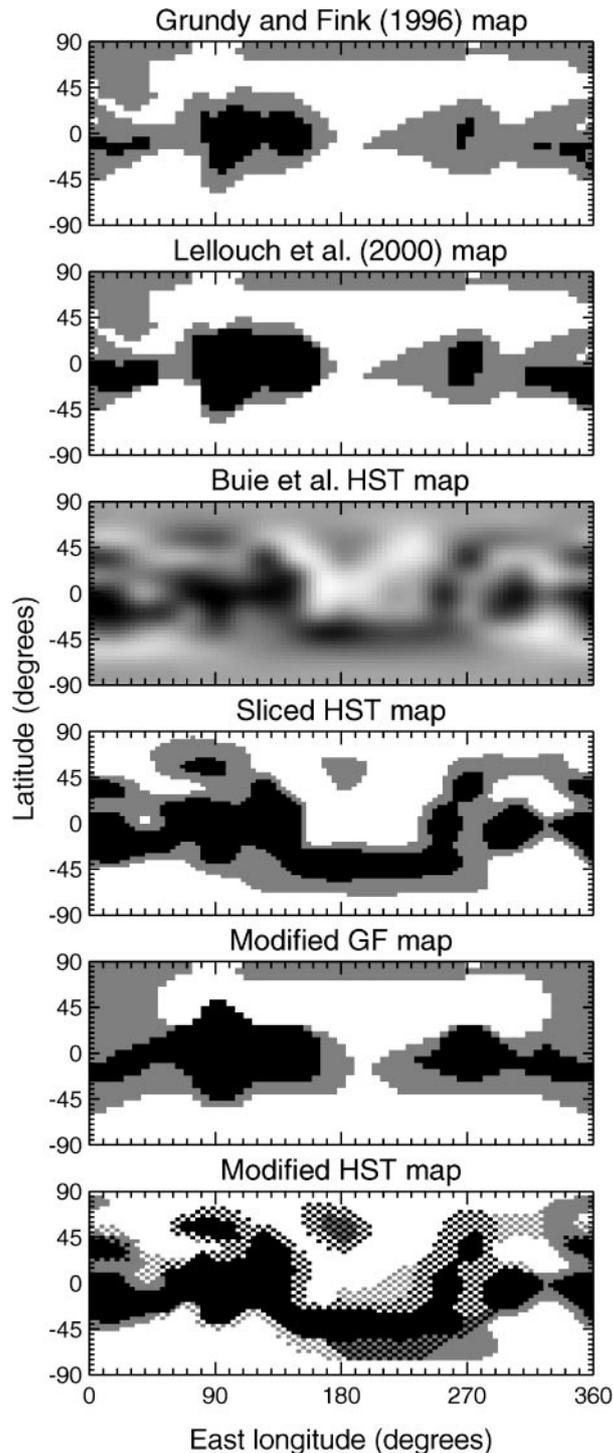

FIG. 10. Pluto maps discussed in this paper, shown in cylindrical projection. White areas are N$_2$-rich terrains, gray areas are CH$_4$-rich terrains, and black areas are H$_2$O/tholin-rich terrains, except in the case of the Buie *et al*. HST map, where shade corresponds to albedo.

variability of one or more of the three Grundy and Fink terrains. One possible scenario could be that the N$_2$-rich terrain is not as uniform as has been supposed. Perhaps there is less CO and CH$_4$ in the region responsible for Pluto's lightcurve maximum but
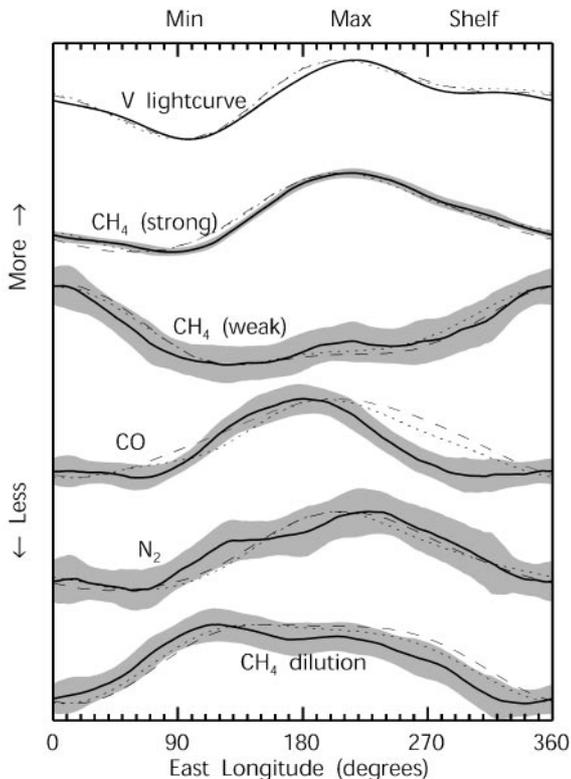
FIG. 11. Observed longitudinal trends (solid curves) compared with predictions of the modified Grundy and Fink map (dashed curves) and modified HST map (dotted curves).

similar spectral trends. Without knowing which effect is responsible for the observed changes in Pluto's spectrum, modeling and interpreting the spectral evolution would be highly speculative, at best. In this section, we will argue that the observed changes in methane band depths are primarily geometric effects, rather than the result of ongoing changes in Pluto's surface ices.

Subsolar (and sub-Earth) latitudes on Pluto have been moving north at about $2°$ per Earth year in recent decades. This slow northward trend will cause secular spectral changes, if the northern and southern hemispheres of Pluto differ spectrally, or if high-latitude regions differ from equatorial ones. Both types of differences are expected, since Pluto's southern hemisphere had been oriented toward the Sun for more than a century up until the mid 1980s, and the northern polar regions have recently begun receiving continuous sunlight for the first time in over a century. A significant quantity of N_2 ice from the southern hemisphere should have sublimated away over the past
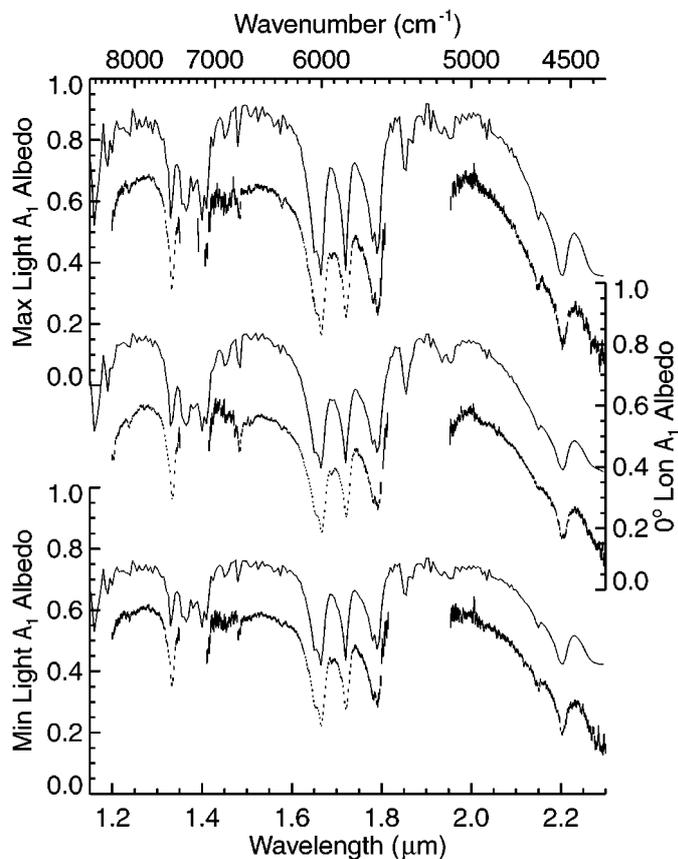
more of these contaminants dissolved in the N_2 ice at other longitudes. Other configurations can be imagined which could equally well explain the observed trends, such as variations in continuum absorption or in vertical compositional gradients within terrains.

An intriguing possibility suggested by the data is that the anomalously bright equatorial patch about longitude $170°$ in the HST map (e.g., the third panel of Fig. 10; see also Stern *et al.* 1997) could be unusually rich in CO ice. How CO could become concentrated in a small, equatorial region is unknown to us, but we note that CO has a significantly higher refractive index than N_2 and CH_4 ices and could thus be more strongly backscattering than Pluto's other ice species, in regions where it was the dominant ice.

Spectral monitoring with higher signal precision will be extremely useful for confirming and refining the trends reported here and could perhaps make it possible to distinguish among various possible scenarios of differentiation of one or more of the three Grundy and Fink terrains.

4.2. Temporal/Latitudinal Distribution

The secular evolution of Pluto's spectrum presents a more challenging problem than the diurnal spectral variations addressed in Section 4.1, because viewing and illumination geometry as well as volatile transport processes could produce

FIG. 12. Examples of theoretical spectra predicted by the modified HST map, for minimum light, $0°$, and maximum light longitudes, and $20°$ latitude (thin curves, offset upward by 0.2). Averages of OSIRIS spectra at comparable geometries are provided for comparison (curves composed of isolated points with error bars). Noise in the highest albedo regions of the model curves results from noise in the laboratory data for CH_4 diluted in N_2 ice. Details of the models used to represent the three terrains are provided in the Appendix.

century, condensing in the northern hemisphere, particularly at high northern latitudes (Benchkoura 1996, Spencer *et al.* 1997, Trafton *et al.* 1998), and likely producing latitude-dependent differences in textures, albedos, and compositions. Various efforts to map albedo features on Pluto's surface are in general agreement that higher northern latitudes have higher albedos on average than albedos in equatorial latitudes (e.g., Buie *et al.* 1992, Young and Binzel 1993, Stern *et al.* 1997, Young *et al.* 1999). Being derived from the albedo maps, our maps share this characteristic.

The previous section showed how band depth variations of the strong CH$_4$ bands were closely correlated with visible albedo variations in longitude, implying that these bands were predominantly formed by CH$_4$ diluted in the bright, N$_2$-rich terrain. If the same correlation holds in latitude, we would expect the strong CH$_4$ bands to become stronger as the viewing geometry shifts toward more northerly sub-Earth latitudes, bringing more of the bright northern terrain into view. This trend of increasing band depths is exactly what is seen in the OSIRIS data. The observed slope measured in Section 3.1 was an increase of $0.6 \pm 0.1\%$ per degree of sub-Earth latitude. We computed spectra for our model maps at a series of sub-Earth latitudes and obtained similar slopes of 0.586% and 0.564% for our modified Grundy and Fink and modified HST maps, respectively.

Unlike the strong CH$_4$ bands, the weak CH$_4$ bands are not formed in the high-albedo N$_2$-rich terrain of our models. They are formed predominantly in darker, CH$_4$-rich regions which are more concentrated at southern and equatorial latitudes. So, as the strong bands increase in depth the weak bands should diminish. This behavior was reported by Grundy and Fink (1996), for the weak 0.73 μm band, based on three matched pairs of observations, each pair spanning a 7-year interval. They reported declines in band strength of 0.4 to 1.4 percent per degree of sub-Earth latitude. Our model maps predict declines in 0.73 μm band depth as well, at rates averaging 0.7 and 0.8 percent per degree of sub-Earth latitude for the modified Grundy and Fink map and the modified HST map, respectively, at the same longitudes and time intervals observed by Grundy and Fink (1996).

The excellent agreement between the theoretical and observed secular trends for both strong and weak CH$_4$ bands is consistent with our hypothesis that the observed behavior is caused by geometric effects, and not by changes in the surface ices themselves. However, several reasons for caution remain to be addressed before we can conclude that the hypothesis is indeed correct.

First, recent photometric observations (Buie and Grundy 2000a) show that Pluto's brightness is gradually diminishing at visible wavelengths, particularly near lightcurve maximum. One possible explanation of this trend could be that high northerly latitudes have low albedos. Another could be that albedos are diminishing with the passage of time. Either scenario conflicts with our picture of northern terrains composed of bright N$_2$-rich ice and a surface distribution of ices and albedos which is static on time scales of a few years. A third explanation could be that

southern middle or high latitudes are bright, and Pluto's dimming results from these regions gradually rotating out of view. That southern mid-latitudes are bright is confirmed by various recent mapping efforts (e.g., Buie *et al.* 1992, Stern *et al.* 1997, Young *et al.* 1999), but if southern high latitudes are also bright, they must have become bright relatively recently to explain Pluto's increasing brightness prior to the 1980s (e.g., Drish *et al.* 1995). It may still be possible to reconcile the lightcurve data with a static albedo pattern if the southern high latitudes are bright, but southern polar regions are quite dark. Whatever the eventual resolution, it is clear that continued photometric and spectroscopic monitoring of Pluto are required to build a convincing case that Pluto's albedo patterns and distribution of volatile ices are not static.

Second, volatile transport calculations by Grundy and Stansberry (2000) and others show that rates of volatile transport should be high enough to significantly alter optically active surface layers of N$_2$-rich regions within a few Earth years, via a process they termed *solar gardening*. The anticipated changes are of sufficient magnitude to be easily observable. In light of the high predicted rate of solar gardening, our attribution of observed changes to geometric effects rather than to the ongoing action of this process demands an explanation. Grundy and Stansberry (2000) argued that solar gardening would either rapidly lead to the establishment of some steady-state configuration or else drive a cycle of evolution which would look like a steady-state when averaged over a sufficiently large geographical extent. Areas on Pluto which have only been exposed to the Sun for a few years and have thus not yet reached the equilibrium state (at present, only north-facing slopes at high northern latitudes) contribute negligibly to the projected surface area seen from Earth, and so the spectral signatures of regions which are currently progressing from winter depositional to summer solar gardened textures would not be easily detected. The visible disk of Pluto is dominated by regions which have been exposed to the Sun for many years, much longer than the predicted time to arrive at a thoroughly solar gardened texture.

While we apparently cannot observe the seasonal onset of solar gardening, we might expect to observe its consequences if the surface configuration of observable N$_2$-rich units represents the product of extensive solar gardening. Grundy and Stansberry (2000) predicted that in solar gardened regions, CH$_4$ ice would become increasing concentrated several centimeters below the surface, where net radiative heating could drive preferential sublimation of N$_2$. The overlaying material, by contrast, would have a composition much closer to the N$_2$-dominated atmosphere, because thermal radiation efficiently cools the uppermost surface of the ice, even at local noon, resulting in surficial condensation of additional ice from the gas phase. Douté *et al.* (1999) demonstrated spectral evidence for the simultaneous existence of terrains including both both N$_2$-rich ice and CH$_4$-rich ice, but their models generally put the CH$_4$-dominated phase on top, because they assumed that sublimation would occur at the uppermost surface.

At weakly absorbing wavelengths, photons penetrate more deeply within a surface than they do at more strongly absorbing wavelengths, providing a way of probing compositional profiles in the optically active layers of Pluto's surface. The absorption coefficients of different near-infrared CH_4 ice bands range over many orders of magnitude (see Table II and Schmitt *et al.* 1998), so that different CH_4 bands are formed, on average, at different depths in the surface of Pluto. Recalling the wavelength shifts discussed in Section 3.5, we can explore CH_4 abundance as a function of depth by comparing the fractions of CH_4 in CH_4-rich versus N_2-rich phases required to fit absorption bands of different strengths. Unfortunately, the large optical path lengths required to produce measurable absorption in the weaker CH_4 bands have hampered laboratory measurements of absorption coefficients for the weaker diluted CH_4 bands. The best laboratory data currently available for diluted CH_4 are those of Quirico and Schmitt (1997a). Fitting the 1.48, 1.33, 1.72, 1.66, and 2.2 μm bands (in order of increasing band depth) to an average of OSIRIS spectra obtained near maximum light, we obtain CH_4-rich fractions of 0.72, 0.37, 0.46, 0.24, and 0.49, respectively. These numbers roughly resemble the anticipated trend, but not exactly. The 2.2 μm band does not fit the trend because that band is considerably broadened and distorted by saturation, leading to spurious fits which prefer fractions of CH_4 in CH_4-rich and in N_2-rich phases to be nearly equal because that combination produces the broadest possible combined absorption band. Probably confusing matters as well are other more subtle problems, such as limitations of the laboratory data which interfere with fits to the weaker 1.48 and 1.33 μm bands. The best-fit CH_4-rich fraction also depends somewhat on the wavelength limits selected and the possible presence of other spectral features. For example, the 1.65 μm water ice band may be contaminating the 1.66 μm CH_4 band to some extent. Further, each band samples a range of surface layers, with deeper strata contributing more to the formation of the wings of each band and more superficial strata controlling the core of each band. Nevertheless, the rough trend seen here suggests that methane is indeed more concentrated below the surface of Pluto, as predicted by Grundy and Stansberry (2000). Alternatively, subsurface enrichment of CH_4 could result from a more CH_4-rich atmospheric composition at the time the ice was deposited, now being revealed by sublimation. To reach a more definitive result, it will be necessary to simultaneously model all wavelengths using a stratified model, which is beyond the scope of this paper.

Returning to the hypothesis of static versus changing ice distributions, we note that there is a simple, direct, Earth-based measurement which could potentially resolve the question. Pluto's motion along its heliocentric orbit currently causes the subsolar latitude on Pluto to move steadily north at a rate of about 2° per Earth year. Near Pluto's perihelion passage, the Earth's motion along its orbit produces a parallax at Pluto's heliocentric distance of ∼4°, aligned approximately along the sky projection of Pluto's spin vector. This parallax provides pairs of opportunities to observe Pluto at one sub-Earth latitude, one during the first

TABLE III
Pairs of OSIRIS Observations

Initial observation			Follow-up observation		
UT date	Lon (°)	Lat (°)	UT date	Lon (°)	Lat (°)
1997/03/24.5	91	20.9	1998/06/27.3	94	21.0
1997/03/25.4	35	20.9	1998/06/28.2	41	21.0
1997/03/26.4	339	20.9	1998/06/29.2	344	21.0
1997/04/15.4	293	20.6	1998/07/19.2	299	20.6

half of an observing season and another during the second half of the following observing season. To fully duplicate the observing (but not the illumination) geometry, one must also observe at the same sub-Earth longitude, which means consideration of Pluto's 6.4-day period. We were also constrained to observe during night time at a fixed terrestrial site. Merging all of these constraints, we found that observations separated by 460 days (1.26 years) provide good duplication of observing geometry. We were fortunate enough to obtain four such pairs in our OSIRIS observations, as tabulated in Table III and circled in Fig. 1.

For each of the four pairs of matched-geometry observations, we measured band depths for four CH_4 bands, at 1.33, 1.66, 1.72, and 2.2 μm. The resulting 32 measured band depths exhibited considerable scatter but were averaged together to obtain a weighted mean change in band depth of $-0.6 \pm 1.3\%$ over the 460-day intervals. This nondetection of a statistically significant change in CH_4 band depths is consistent with none of the observed secular evolution being due to volatile transport. The $-0.6 \pm 1.3\%$ number can be compared with the expected change of $+1.5 \pm 0.3\%$ in 460 days (based on the observed secular change of $+0.6 \pm 0.1\%$ per degree of latitude, assuming all of the change was due to ice evolution instead of viewing geometry). The signal precision of our OSIRIS data is only sufficient to exclude the changing ice model at the 1.4 σ confidence level. This experiment needs to be repeated with an instrument capable of delivering higher signal precision, and similar experiments could also be done at CCD wavelengths.

5. CONCLUSION

We present 83 new near-infrared spectra of Pluto, obtained during 1995–1998 at Lowell Observatory's Perkins telescope. The new data sketch a uniquely detailed picture of the physical distribution of CO, N_2, and CH_4 ices on Pluto's surface. Specifically, the new data have enabled us to:

• explore the close correlation between strong near-infrared CH_4 band depths and Pluto's visible lightcurve in much greater detail than earlier efforts,

• show that N_2 absorption does not correlate with the visible lightcurve, by means of the 0-2 band at 2.15 μm,

• show that CO absorption does not correlate with the visible lightcurve and has a narrow absorption peak near 170° longitude,

from measurement of the 0-3 band at 1.579 μm (the CO absorption maximum seems to coincide with an anomalously bright, equatorial spot on Pluto's surface),

• independently confirm the existence of two distinct units containing CH$_4$ ice, based on contrasting longitudinal behavior and secular trends between weak and strong CH$_4$ bands,

• show that CH$_4$ dilution correlates with N$_2$ optical path length, but not with the visible lightcurve, by directly measuring variations in CH$_4$ dilution in N$_2$ ice with longitude,

• independently confirm and refine the general geographic distribution of CH$_4$ and N$_2$:CH$_4$ ices proposed by Grundy and Fink (1996),

• detect a secular trend of increasing band depth in stronger CH$_4$ bands, consistent with a geometric explanation and not requiring the spatial distribution of Pluto's ices to have changed over the 1995–1998 interval.

The data also raise some puzzling new questions. For example, the secular trends of increasing depths of strong CH$_4$ bands and declining depths of weak CH$_4$ bands suggests that Pluto's high northern latitudes are predominantly surfaced with N$_2$: CH$_4$: CO solid solution, consistent with expectation from volatile transport models. However, photometric observations imply that these regions may be be darker than N$_2$-rich terrains at lower latitudes. It is not clear why high northern latitude N$_2$ ice should be darker. Additional photometric and spectroscopic observations are needed to resolve this puzzle. Perhaps the northern high latitudes have darkened since the mutual event season, due to the ongoing action of processes such as solar gardening. The north polar regions may be quite unusual, compared with other parts of Pluto's surface. Unlike lower latitudes which have received daytime sunlight for many decades, north polar regions emerged into continuous, perihelion sunlight in the mid 1980s, after more than a century of continuous darkness. Depositional processes associated with condensation on the dark winter hemisphere would have been suddenly supplanted by solar gardening/sublimation type processes. The textures and compositional distribution of ices near the pole may still reflect this recent, abrupt shift in dominant processes.

Finally, we must stress how essential it is to repeatedly obtain diverse types of data over time scales which provide *dense temporal sampling* of Pluto's diurnal and seasonal variability. Of particular value are visible wavelength photometry, visible to near-infrared spectroscopy, and thermal infrared photometry. Only by bringing together well-sampled data of these different types can real breakthroughs be made in understanding the remarkably complex surface of the ninth planet.

Much more *dense spatial sampling* is an essential counterpart to the dense temporal sampling we call for. The kind of spatial resolution needed can only realistically be achieved by a spacecraft visit to the Pluto/Charon system. Sending a spacecraft will yield enormous scientific benefits, but it must be done quickly or the scientific return will be diminished by simple geometry. As subsolar latitudes on Pluto continue marching northward, more and more of the planet's southern hemisphere moves into permanent shadow, beyond the reach of traditional spacecraft imaging experiments for the remainder of the century. In planning a spacecraft flyby, it will be essential to consider the distribution of ices implied by our data. If flyby timing is not carefully optimized with respect to Pluto longitude, a single spacecraft may be unable to do high-resolution imaging of some of Pluto's distinct provinces, thus falling short of its scientific potential to provide geological context for all of Pluto's diverse terrain types.

APPENDIX

Model Configuration of Pluto's Three Terrain Types

In modeling the three terrains proposed by Grundy and Fink (1996), we have slightly modified their configurations to improve agreement with our new near-infrared spectra, to add CO ice, and to bring the model's photometric phase curve into agreement with the value reported by Buie *et al.* (1997). It is certain that better fits to the spectra could be obtained by additional adjustment of our model terrains, but our primary objective is understanding the sources of Pluto's spectral variations, not achieving a cosmetically perfect spectral match. The Hapke parameters adopted for this paper are macroscopic roughness $\bar{\theta} = 10°$, backscattering parameter $B_0 = 0.8$, compaction parameter $h = 0.1$, and a single-scattering phase function $P_{(g)}$ composed of a two-term Henyey–Greenstein phase function with width parameter $b = 0.63$ and asymmetry parameter $c = -0.6$ (using the parameterization of McGuire and Hapke (1995)). These values are not unique in providing a match to the Buie *et al.* (1997) phase curve, but they are plausible values for transparent, icy grains and are comparable to parameters fitted to Voyager photometry of Triton and other outer Solar System objects. It is unreasonable to expect these parameters to be constants, neither dependent on wavelength nor on terrain type, but not having additional constraints to apply we must make gross assumptions.

The first terrain is an exceptionally bright one, dominated by N$_2$ ice, with small quantities of CH$_4$ and CO ice mixed into the N$_2$ ice in solid solution, as envisioned by Lunine and Stevenson (1985). Large portions of Triton's surface (Eluszkiewicz 1991, Cruikshank *et al.* 1993, Quirico *et al.* 1999) are probably similar to this unit. Our model for Pluto's N$_2$-rich terrain is produced by combining β N$_2$ ice at 37 K with 0.7% diluted CH$_4$ ice, 0.15% diluted CO ice, and 0.000003% tholin (volumetric proportions). Optical constants for the N$_2$ ice were taken from Grundy *et al.* (1993), for the diluted CH$_4$ ice from Quirico and Schmitt (1997a), and for the tholin from Khare *et al.* (1984). Since optical constants for the 0-3 band of diluted CO ice were not available, we used the Legay-Sommaire and Legay (1982) data for pure CO and adjusted it according to the observed differences between the 0-2 bands in pure and diluted CO (Quirico and Schmitt 1997b). Peak absorption coefficients for β N$_2$ and diluted CO are included in Table II. In addition to the linear combination of these optical constants, we imposed a minimum absorption coefficient of 0.0003 cm^{-1}, to overcome problems where noisy optical constants near zero go negative, resulting in meaningless single-scattering albedos. The choice of 37 K temperature for the nitrogen ice is based on modeling by Douté *et al.* (1999), as well as radiative balance modeling by Grundy and Stansberry (2000). We used 10-cm-diameter "grains," as done by Douté *et al.* (1999). Much heated discussion has surrounded the issue of grain sizes in Hapke models. The problem is that backscattering single-scattering phase functions are required to match the observed photometric behavior of bodies such as Triton, yet individual crystals of nitrogen ice are invariably forward scattering, owing to their feeble absorption coefficients and small refractive indices. The "grains" simulated in our models should probably be thought of as aggregates of numerous smaller particles, these subparticles being most likely in the several millimeter size range.

The next terrain has no analog on Triton, being dominated by CH$_4$ ice. This terrain could perhaps be produced by sublimation of most of the nitrogen from the previous terrain. In addition to spectroscopic evidence, its occurrence is supported by two-component volatile transport models (e.g., Benchkoura 1996), as well as the high CH$_4$ abundance in Pluto's atmosphere (e.g., Stansberry

et al. 1996). ISO thermal infrared observations suggest that this terrain has a low thermal inertia and significant diurnal temperature variations (Lellouch *et al.* 2000), implying limited diurnal sublimation and condensation of N_2 in this terrain. Nitrogen may still be present, dissolved in the CH_4 ice as a minority species, but it is not expected to be spectroscopically detectable. No laboratory data are available for near-infrared spectral behavior of CH_4 ice with dissolved N_2. Consequently, we simulated Pluto's CH_4-rich terrain with pure, granular CH_4 ice at 40 K with 0.0002% tholin dispersed through the CH_4 to simulate radiation-induced production of tholin in the CH_4 ice (e.g., Strazzulla *et al.* 1984, Stern *et al.* 1988, Johnson 1989). CH_4 ice optical constants were taken from a data set currently being prepared for publication (three preliminary spectra were published by Schmitt *et al.* (1998)). Selected CH_4 ice peak absorption coefficients are included in Table II. The tholin optical constants were taken from Khare *et al.* (1984). We also imposed a minimum absorption coefficient of 0.04 cm^{-1}. Instead of having a single grain size of this material, we found that our spectral fits were improved by using a mixture of 1 cm and 0.1 mm grains, mixed in the proportions 99.5% and 0.5%, respectively (by volume). The smaller grains served to scatter light into the cores of the stronger, saturated absorption bands, broadening them relative to the band widths in models composed of a single grain size. An alternative way of interpreting such a mixture of grain sizes is to think of the small grains as representing rough texture on the surfaces of the large ice grains.

The last terrain is dark, reddish, and rich in nonvolatile H_2O ice and organic tholins. This terrain is hypothesized to underlie other terrains on Pluto, being exposed wherever N_2, CO, and CH_4 ices have sublimated away, leaving only the photolytic and radiolytic residues which accumulate in the ice and/or settle out of the atmosphere. The centaur 5145 Pholus is a potential spectral analog (e.g., Cruikshank *et al.* 1998). To simulate this terrain, we used a granular/intimate mixture consisting of 70% (by volume) 70 μm grains of crystalline H_2O ice I_h at 50 K, 15% 3 μm grains of tholin, and 15% 3 μm grains of opaque carbon. Optical constants for the H_2O ice were taken from Grundy and Schmitt (1998) and for the tholin from Khare *et al.* (1984). Opaque carbon was simulated by using a refractive index of 1 and an absorption coefficient of 10,000 cm^{-1}. This seemingly strange approximation is necessitated by a limitation of the equivalent slab model used to compute single-scattering albedos in our implementation of the Hapke model. The equivalent slab model fails to duplicate the optical behavior of actual carbon grains because real carbon particles are rough at the scale of the wavelength of light, enabling more light than the equivalent slab model predicts to penetrate into the grains and thus be absorbed. If the optical constants of amorphous carbon were used instead of our ad hoc numbers, the equivalent slab model would incorrectly predict high single-scattering albedos, because of specular reflection from the grain's exterior.

ACKNOWLEDGMENTS

REFERENCES

Benchkoura, A. I. 1996. *Modelisation du transport de volatils à la surface des planètes et satellites glacés du systeme solaire: Application à Triton et Pluton.* Ph.D. thesis, Univ. Joseph Fourier, Grenoble.

Buie, M. W., and U. Fink 1987. Methane absorption variations in the spectrum of Pluto. *Icarus* **70**, 483–498.

Buie, M. W., and W. M. Grundy 2000a. Continuing evolution of the lightcurve of Pluto. *Bull. Am. Astron. Soc.* **32**, 1083 (abstract).

Buie, M. W., and W. M. Grundy 2000b. The distribution and physical state of H_2O on Charon. *Icarus* **148**, 324–339.

Buie, M. W., D. J. Tholen, and K. Horne 1992. Albedo maps of Pluto and Charon: Initial mutual event results. *Icarus* **97**, 211–227.

Buie, M. W., D. J. Tholen, and L. H. Wasserman 1997. Separate lightcurves of Pluto and Charon. *Icarus* **125**, 233–244.

Buratti, B. J., M. D. Hicks, and R. L. Newburn Jr. 1999. Does global warming make Triton blush? *Nature* **397**, 219.

Cleveland, W. S. 1979. Robust locally weighted regression and smoothing scatterplots. *J. Am. Stat. Assoc.* **74**, 829–836.

Cruikshank, D. P., T. L. Roush, T. C. Owen, T. R. Geballe, C. de Bergh, B. Schmitt, R. H. Brown, and M. J. Bartholomew 1993. Ices on the surface of Triton. *Science* **261**, 742–745.

Cruikshank, D. P., T. L. Roush, J. M. Moore, M. V. Sykes, T. C. Owen, M. J. Bartholomew, R. H. Brown, and K. A. Tryka 1997. The surfaces of Pluto and Charon. In *Pluto and Charon* (S. A. Stern and D. J. Tholin, Eds.), pp. 221–267. Univ. of Arizona Press, Tucson.

Cruikshank, D. P., T. L. Roush, M. J. Bartholomew, T. R. Geballe, Y. J. Pendleton, S. M. White, J. F. Bell III, J. K. Davies, T. C. Owen, C. de Bergh, D. J. Tholen, M. P. Bernstein, R. H. Brown, K. A. Tryka, and C. M. Dalle Ore 1998. The composition of centaur 5145 Pholus. *Icarus* **135**, 389–407.

DePoy, D. L., B. Atwood, P. Byard, J. Frogel, and T. O'Brien 1993. Infrared imager/spectrometer (OSIRIS). *Proc. SPIE* **1946**, 667–672.

Douté, S., B. Schmitt, E. Quirico, T. C. Owen, D. P. Cruikshank, C. de Bergh, T. R. Geballe, and T. L. Roush 1999. Evidence for methane segregation at the surface of Pluto. *Icarus* **142**, 421–444.

Drish, W. F., R. Harmon, R. L. Marcialis, and W. J. Wild 1995. Images of Pluto generated by matrix lightcurve inversion. *Icarus* **113**, 360–386.

Eluszkiewicz, J. 1991. On the microphysical state of the surface of Triton. *J. Geophys. Res.* **96**, 19219–19229.

Grundy, W. M. 1995. *Methane and Nitrogen Ices on Pluto and Triton: A Combined Laboratory and Telescope Investigation.* Ph.D. thesis, Univ. of Arizona, Tucson.

Grundy, W. M., and U. Fink 1996. Synoptic CCD spectrophotometry of Pluto over the past 15 years. *Icarus* **124**, 329–343.

Grundy, W. M., and B. Schmitt 1998. The temperature-dependent near- infrared absorption spectrum of hexagonal H_2O ice. *J. Geophys. Res.* **103**, 25809–25822.

Grundy, W. M., and J. A. Stansberry 2000. Solar gardening and the seasonal evolution of nitrogen ice on Triton and Pluto. *Icarus* **148**, 340–346.

Grundy, W. M., B. Schmitt, and E. Quirico 1993. The temperature dependent spectra of α and β nitrogen ice with application to Triton. *Icarus* **105**, 254–258.

Grundy, W. M., M. W. Buie, J. A. Stansberry, J. R. Spencer, and B. Schmitt 1999. Near-infrared spectra of icy outer solar system surfaces: Remote determination of H_2O ice temperatures. *Icarus* **142**, 536–549.

Hapke, B. 1993. *Theory of Reflectance and Emittance Spectroscopy.* Cambridge Univ. Press, New York.

Hilbert, B. N., J. A. Stansberry, W. M. Grundy, R. V. Yelle, M. W. Buie, C. Dalla Piazza 1998. Search for secular changes in the near-infrared spectrum of Triton. *Bull. Am. Astron. Soc.* **30**, 1108 (abstract).

Hilbert, B. N., J. A. Stansberry, W. M. Grundy, M. W. Buie, and R. V. Yelle 1999. The near-IR spectrum of Triton: Characterization and search for variability. Paper presented at Pluto & Triton, September 23–24, Flagstaff, AZ.

Johnson, R. E. 1989. Effect of radiation on the surface of Pluto. *Geophys. Res. Lett.* **16**, 1233–1236.

Khare, B. N., C. Sagan, E. T. Arakawa, F. Suits, T. A. Callcott, and M. W. Williams 1984. Optical constants of organic tholins produced in a simulated

Titanian atmosphere: From soft X-ray to microwave frequencies. *Icarus* **60**, 127–137.

Legay-Sommaire, N., and F. Legay 1982. Analysis of the infrared emission and absorption spectra from isotopic CO molecules in solid α-CO. *Chem. Phys.* **66**, 315–325.

Lellouch, E., R. Laureijs, B. Schmitt, E. Quirico, C. de Bergh, J. Crovisier, and A. Coustenis 2000. Pluto's non isothermal surface. *Icarus* **147**, 220–250.

Lunine, J. I., and D. J. Stevenson 1985. Physical state of volatiles on the surface of Triton. *Nature* **317**, 238–240.

Marcialis, R. L. 1997. The first 50 years of Pluto–Charon research. In *Pluto and Charon* (S. A. Stern and D. J. Tholin, Eds.), pp. 27–83. Univ. of Arizona Press, Tucson.

Marcialis, R. L., and L. A. Lebofsky (1991). CVF spectrophotometry of Pluto: Correlation of composition with albedo. *Icarus* **89**, 255–263.

McGuire, A. F., and B. W. Hapke 1995. An experimental study of light scattering by large, irregular particles. *Icarus* **113**, 134–155.

Owen T. C., T. L. Roush, D. P. Cruikshank, J. L. Elliot, L. A. Young, C. de Bergh, B. Schmitt, T. R. Geballe, R. H. Brown, and M. J. Bartholomew 1993. Surface ices and atmospheric composition of Pluto. *Science* **261**, 745–748.

Porto de Mello, G. F., and L. da Silva 1997. HR 6060: The closest ever solar twin? *Astrophys. J.* **482**, L89–92.

Quirico, E. 1995. *Etudes spectroscopiques proche infrarouges de solides moléculaires: Application à l'étude des surfaces glacées de Triton et Pluton*. Ph.D. dissertation, Univ. Joseph Fourier, Grenoble.

Quirico, E., and B. Schmitt 1997a. Near-infrared spectroscopy of simple hydrocarbons and carbon oxides diluted in solid N$_2$ and as pure ices: Implications for Triton and Pluto. *Icarus* **127**, 354–378.

Quirico, E., and B. Schmitt 1997b. A spectroscopic study of CO diluted in N$_2$ ice: Applications for Triton and Pluto. *Icarus* **128**, 181–188.

Quirico, E., S. Douté, B. Schmitt, C. de Bergh, D. P. Cruikshank, T. C. Owen, T. R. Geballe, and T. L. Roush 1999. Composition, physical state, and distribution of ices at the surface of Triton. *Icarus* **139**, 159–178.

Schmitt, B., E. Quirico, F. Trotta, and W. M. Grundy 1998. Optical properties of ices from UV to infrared. In *Solar System Ices* (B. Schmitt, C. de Bergh, and M. Festou, Eds.), pp. 199–240. Kluwer Academic, Boston.

Spencer, J. R., J. A. Stansberry, L. M. Trafton, E. F. Young, R. P. Binzel, and S. K. Croft 1997. Volatile transport, seasonal cycles, and atmospheric dynamics on Pluto. In *Pluto and Charon* (S. A. Stern and D. J. Tholen, Eds.), pp. 435–473. Univ. of Arizona Press, Tucson.

Stansberry, J. A., J. R. Spencer, B. Schmitt, A. Benchkoura, R. V. Yelle, and J. I. Lunine 1996. A model for the overabundance of methane in the atmospheres of Pluto and Triton. *Planet. Space Sci.* **44**, 1051–1063.

Stern, S. A., L. M. Trafton, and G. R. Gladstone 1988. Why is Pluto bright? Implications of the albedo and lightcurve behavior of Pluto. *Icarus* **75**, 485–498.

Stern, S. A., M. W. Buie, and L. M. Trafton 1997. High resolution images and maps of Pluto. *Astron. J.* **113**, 827–843.

Strazzulla, G., L. Calcagno, and G. Foti 1984. Build up of carbonaceous material by fast protons on Pluto and Triton. *Astron. Astrophys.* **140**, 441–444.

Trafton, L., D. L. Matson, and J. A. Stansberry 1998. Surface/atmosphere interaction and volatile transport (Triton, Pluto, Io). In *Solar System Ices* (B. Schmitt, C. de Bergh, and M. Festou, Eds.), pp. 773–812. Astrophys. Space Sci. Library. Kluwer Academic, Boston.

Trafton, L. A. 1999. On the phases of N$_2$ and CH$_4$ ices on Pluto vs Triton. Paper presented at Pluto & Triton, September 23–24 Flagstaff, AZ.

Young, E. F., and R. P. Binzel 1993. Comparative mapping of Pluto's sub-Charon hemisphere: Three least squares models based on mutual event lightcurves. *Icarus* **102**, 134–149.

Young, E. F., K. Galdamez, M. W. Buie, R. P. Binzel, and D. J. Tholen 1999. Mapping the variegated surface of Pluto. *Astron. J.* **117**, 1063–1076.